

THE DYNAMICAL STATE OF THE FRONTIER FIELDS GALAXY CLUSTER ABELL 370

SANDOR M. MOLNAR¹, SHUTARO UEDA¹, AND KEIICHI UMETSU¹

Draft version August 4, 2020

ABSTRACT

We study the dynamics of Abell 370 (A370), a highly massive Hubble Frontier Fields galaxy cluster, using self-consistent three-dimensional N -body/hydrodynamical simulations. Our simulations are constrained by X-ray, optical spectroscopic and gravitational lensing, and Sunyaev–Zel’dovich (SZ) effect observations. Analyzing archival *Chandra* observations of A370 and comparing the X-ray morphology to the latest gravitational lensing mass reconstruction, we find offsets of ~ 30 kpc and ~ 100 kpc between the two X-ray surface brightness peaks and their nearest mass surface density peaks, suggesting that it is a merging system, in agreement with previous studies. Based on our dedicated binary cluster merger simulations, we find that initial conditions of the two progenitors with virial masses of $1.7 \times 10^{15} M_{\odot}$ and $1.6 \times 10^{15} M_{\odot}$, an infall velocity of 3500 km s^{-1} , and an impact parameter of 100 kpc can explain the positions and the offsets between the peaks of the X-ray emission and mass surface density, the amplitude of the integrated SZ signal, and the observed relative line-of-sight velocity. Moreover, our best model reproduces the observed velocity dispersion of cluster member galaxies, which supports the large total mass of A370 derived from weak lensing. Our simulations strongly suggest that A370 is a post major merger after the second core passage in the infalling phase, just before the third core passage. In this phase, the gas has not settled down in the gravitational potential well of the cluster, which explains why A370 does not follow closely the galaxy cluster scaling relations.

Keywords: galaxies: clusters: general – galaxies: clusters: individual (Abell 370) – methods: numerical

1. INTRODUCTION

Abell 370 (A370) is a well-studied galaxy cluster at a redshift of $z = 0.375$ (e.g., Tyson et al. 1990; Kochanek et al. 1990; Miralda-Escude 1991; Umetsu et al. 1999; Medezinski et al. 2010; Schmidt et al. 2014; Treu et al. 2015; Lagattuta et al. 2017; Lotz et al. 2017; Lagattuta et al. 2019, and references therein). It was one of the first galaxy clusters in which gravitational lensing was observed (Soucail 1987). The first spectroscopically confirmed giant arc was also discovered in this cluster (Soucail et al. 1988). A370 was found to be one of the most massive clusters based on weak gravitational lensing, with a total virial mass of $M_{\text{vir}} \approx 3.3 \times 10^{15} M_{\odot}$ (Umetsu et al. 2011a,b). Because of its large projected mass and high lensing magnification capability of background galaxies, A370 has been known as a *superlens* characterized by large Einstein radii (e.g., $\theta_{\text{Ein}} > 30''$ for $z_s = 2$; Broadhurst et al. 2008), and selected as one of the six Hubble Frontier Fields² clusters (Lotz et al. 2017). More recently, A370 has been targeted by the BUFFALO survey (Steinhardt et al. 2020) with *Hubble Space Telescope* (*HST*), which will expand the existing area coverage of the Hubble Frontier Fields in optical and near-infrared pass bands.

The mass surface density, the galaxy number density, and X-ray surface brightness show a symmetric bimodal distribution along the north-south direction in the core of A370, suggesting that it is a massive major merger with a mass ratio close to unity (Richard et al. 2010; Lagattuta et al. 2017; Strait et al. 2018; Diego et al. 2018). Two brightest cluster galaxies (BCGs) were found in the core of A370. The BCG located in the south of the core of the cluster is very close to the mass peak of the southern cluster component (within a few kpc), while the northern BCG shows a significant offset from

the northern cluster mass peak (~ 50 kpc; e.g., Richard et al. 2010; Strait et al. 2018). Botteon et al. (2018) used X-ray observations of A370 to search for surface brightness discontinuities to identify shocks and contact discontinuities. They found evidence for surface brightness edges on the western and the eastern side of the cluster. Although the origin of the surface brightness edges is not clear, the edges might be associated with shocks induced by a merger.

Galaxy cluster scaling relations applied to A370 also point to its dynamical activity. Based on the total mass M_{500} (all relevant symbols are defined in detail at the end of this section) estimated from weak lensing (Umetsu et al. 2011a), the X-ray luminosity in the 0.5 – 2 keV band is a factor of ~ 2 –3 times smaller than that inferred from the L_X – M_{500} scaling relation of Pratt et al. (2009). Moreover, M_{500} estimated by *Planck* Sunyaev–Zel’dovich (SZ) effect observations is a factor of ~ 2.5 smaller than the weak-lensing mass (Umetsu et al. 2011a; Coe et al. 2019). All of these pieces of evidence, namely the discrepancies in mass scaling relations, positional offsets between the galaxy and mass surface densities, and multiple X-ray brightness peaks, imply dynamical activity in the cluster.

Motivated by these observational results, here we carry out the first attempt to model A370 as a binary major merger by performing dedicated numerical simulations on CPU clusters using our three-dimensional (3D) N -body/hydrodynamical code based on FLASH (Molnar et al. 2012, 2013a,b; Molnar & Broadhurst 2015, 2017, 2018) developed at the University of Chicago (Fryxell et al. 2000).

The structure of this paper is as follows. In Section 2, we summarize the results from multi-wavelength observations of A370 including our results based on re-analyzing existing *Chandra* X-ray observations. We describe our simulation setup to obtain a model of A370 as a binary merger in Section 3. Section 4 presents our results from hydrodynamical modeling of A370. Section 5 contains our summary.

¹ Institute of Astronomy and Astrophysics, Academia Sinica, No. 1, Section 4, Roosevelt Road, Taipei 10617, Taiwan, R.O.C.

² <https://frontierfields.org>

We adopt a spatially flat, cosmological-constant and dark-matter dominated (Λ CDM) cosmology with $h = 0.7$, $\Omega_m = 0.3$, and $\Omega_\Lambda = 0.7$. We use the standard notation M_Δ to denote the mass enclosed within a sphere of radius R_Δ , within which the mean overdensity equals Δ times the cosmic critical density $\rho_c(z)$ at the cluster redshift z . We adopt the virial overdensity $\Delta \simeq 128$ (i.e., $M_{\text{vir}} \simeq M_{128}$) based on the spherical collapse model (see Appendix A of [Kitayama & Suto 1996](#)). The quoted errors represent the 68% confidence level, unless stated otherwise.

2. MULTI-WAVELENGTH OBSERVATIONS OF A370

2.1. X-ray observations

High angular resolution ($\sim 1''$) X-ray observations provide critical constraints on N -body/hydrodynamical simulations because the X-ray emission traces the intracluster gas. In principle, thermal SZ observations could also be used to map the intracluster gas structure. Although recent SZ observations are reaching the necessary angular resolution (e.g., ALMA), spatially resolved SZ observations are limited to a handful of clusters. Therefore, in practice, X-ray observations are used for simulations to constrain the gas distribution (e.g., [Molnar 2016](#)).

Since X-ray observations are essential to set up our simulations, we have reanalyzed the publicly available *Chandra* observations of A370. The cluster was observed with Advanced CCD Imaging Spectrometer (ACIS) ACIS-S (ObsID = 515) and ACIS-I (ObsID = 7715) with exposure times of 90 ksec and 7 ksec. The first observation with a long exposure time was performed in Cycle 1, when the focal plane temperature was warmer than the standard -119.7°C . The Charge Transfer Inefficiency (CTI) correction is valid for a focal-plane temperature of $\sim -120^\circ\text{C}$. Charge transfer inefficiency degrades the spectral resolution of the instruments. Unfortunately no CTI correction is available for Cycle 1 observations, thus this correction cannot be performed on these ACIS-S observations (e.g., [Botteon et al. 2018](#)). Therefore, we do not use X-ray temperature information, only morphology as a constraint on our FLASH simulations.

We followed standard data reduction and cleaning procedures using the updated versions 4.9 of Chandra Interactive Analysis of Observations (CIAO; [Fruscione et al. 2006](#)) and version 4.7.8 of the calibration database (CALDB; for details of our procedure see [Ueda et al. 2019](#)). After cleaning the data, the remaining exposure time was 70 ksec. The background data were extracted from the region between $3.4'$ and $6.0'$ from the X-ray peak position (marking the cluster center) only on ACIS-S3 chip. The Galactic absorption was fixed at $3.01 \times 10^{20} \text{ cm}^{-2}$ ([Kalbera et al. 2005](#)).

In [Figure 1](#), we show the resulting exposure-corrected and background-subtracted X-ray surface brightness distribution (see also the first panel in [Figure 3](#)). We smoothed the X-ray image using a Gaussian with a constant width ($5''$) because adaptive smoothing may bring out non-existing structures in low surface brightness regions. The point source in the north is a foreground X-ray bright elliptical galaxy at $z = 0.044$. The two black crosses mark the peak positions of the two dark-matter halos derived from a strong-lensing analysis ([Strait et al. 2018](#)).

The X-ray surface brightness distribution is strongly elongated in the north-south direction, showing a disturbed morphology with two peaks ([Figure 1](#)). The brightest X-ray peak is located about half way between the two mass centers, east-

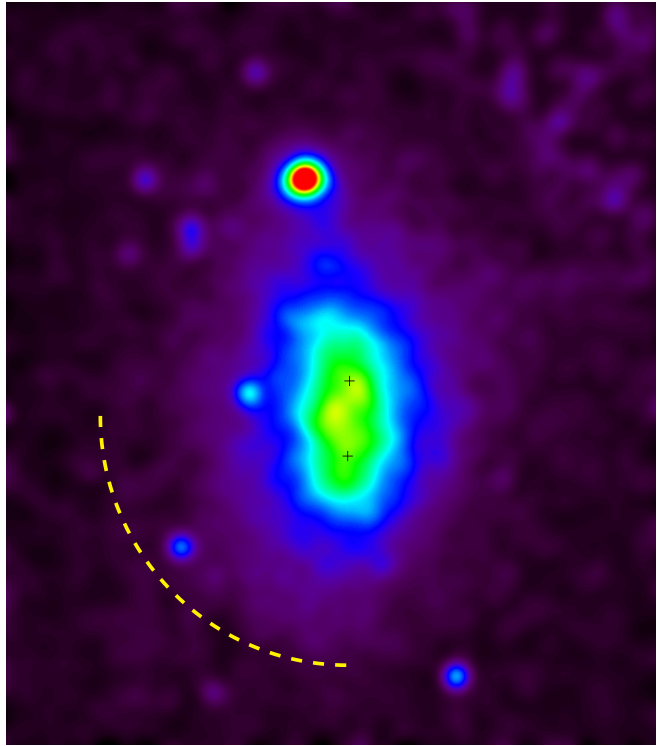


Figure 1. Smoothed X-ray surface brightness image of A370 based on *Chandra* ACIS data. The bright X-ray source in the north is a foreground elliptical galaxy. The two black crosses correspond to the peak positions of dark-matter halos derived from strong gravitational lensing ([Strait et al. 2018](#)). The image size is $1.8 \text{ Mpc} \times 2.0 \text{ Mpc}$. The yellow dashed line represents the surface brightness edge found in this study, in agreement with [Botteon et al. \(2018\)](#).

ward of the lines connected them at a distance of $\sim 100 \text{ kpc}$. The northern X-ray peak is located south-west of the northern mass peak by about 30 kpc . Disturbed X-ray morphology and offsets between X-ray and mass peaks are clear signs of dynamical activity. As demonstrated in [Molnar et al. \(2012\)](#), these offsets can be used to constrain the dynamical state of a merging cluster.

Fitting two broken power-law models to the X-ray surface brightness of A370, we found a drop in the X-ray emission at $690_{-30}^{+60} \text{ kpc}$ to the east of the cluster center (yellow dashed line in [Figure 1](#)), in agreement with [Botteon et al. \(2018\)](#), but found no significant edge on the west side.

2.2. Radio Observations

We carried out a series of SZ observations of 45 galaxy clusters in the Bolocam X-ray SZ (BOXSZ) sample using Bolocam at 140 GHz at the Caltech Submillimeter Observatory ([Czikon et al. 2015](#)). We found an integrated SZ amplitude within R_{2500} of $Y_{2500} = (0.91 \pm 0.16) \times 10^{-10} \text{ ster}$ in A370 (see Table 3 of [Czikon et al. 2015](#)). Since the angular resolution of Bolocam at 140 GHz is $45''$, we use only the amplitude of the SZ signal. For morphology, we use the *Chandra* image to constrain our FLASH simulations.

2.3. Optical Observations

[Umetsu et al. \(2011a\)](#) presented a wide-field weak-lensing analysis of 5 superlens clusters (A1689, A1703, A370, Cl0024+17, RXJ1347-11) based on Subaru telescope observations. By combining the Subaru weak-lensing constraints with their strong-lensing mass profile derived from *HST* data

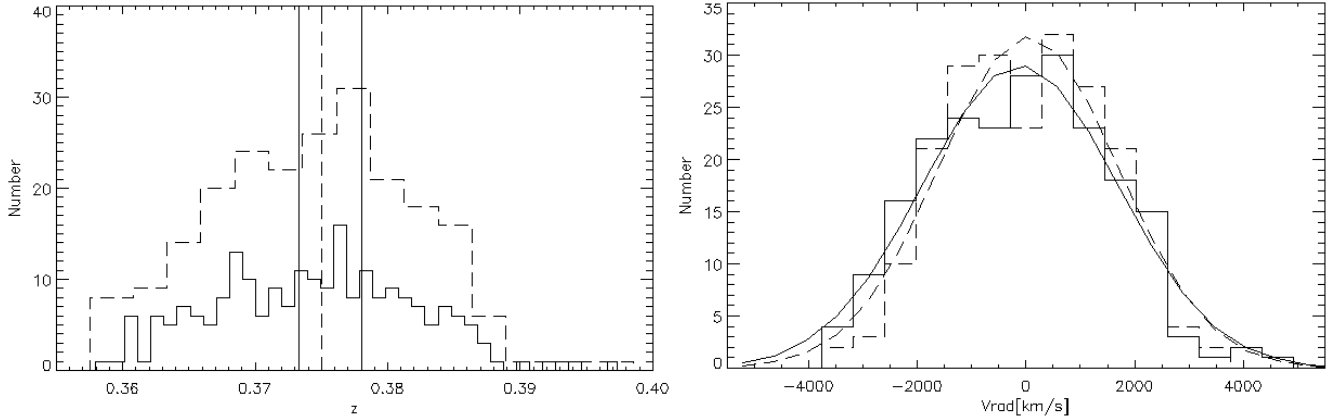


Figure 2. Left panel: Redshift distribution of cluster member galaxies in A370 from Lagattuta et al. (2019) using different bin sizes (solid and dashed histograms). The cluster redshift (0.3750) and the redshifts of the two BCGs (0.3733 and 0.3780), are marked with dashed and solid vertical lines. Right panel: Relative radial velocity distribution in A370 (histograms) and Gaussian fits (curves) from observations and simulations (solid and dashed lines).

(see also Umetsu et al. 2011b), Umetsu et al. (2011a) obtained a virial mass of $M_{\text{vir}} = 3.25_{-0.314}^{+0.364} \times 10^{15} M_{\odot}$ and a concentration of 5.68 ± 0.48 for A370 (see their Table 6), assuming a generalized form of the Navarro–Frenk–White density profile (Navarro, Frenk & White 1997, hereafter NFW).

In agreement with earlier studies, recent strong-lensing reconstructions of the mass surface density distribution and critical curves in the cluster core reveal a symmetric bimodal mass distribution elongated in the north-south direction (Strait et al. 2018; Diego et al. 2018; Lagattuta et al. 2019). The critical curves derived recently are quite similar (Figure 5 of Strait et al. 2018) and compatible with the assumption that A370 is a merging system of two massive clusters. However, these strong-lensing studies identified different numbers of dark matter components in the central region, one (Diego et al. 2018), two (Strait et al. 2018), or three (Lagattuta et al. 2019). Only two BCGs were found in the center of A370, which suggests that A370 is a binary merger. Strait et al. (2018) used a method combining weak and strong lensing, finding two main mass peaks and a few less significant peaks that are likely associated with substructure. Thus, we assume here that A370 is a massive binary merger and adopt a projected distance between the two mass centers of $D_{\text{proj}} = 206$ kpc (Strait et al. 2018). The peak positions of two main dark matter halos (north and south) were precisely constrained by strong-lens modeling based on a large set of multiple images of background galaxies, albeit model dependent. We thus consider only a ± 30 kpc change in D_{proj} . The symmetry in the mass distribution implies that the ratio of the total masses of the two colliding clusters was close to unity, $M_1/M_2 \sim 1$.

Based on optical spectroscopy of a few cluster member galaxies, a relative radial velocity between the northern and southern components was estimated to be $V_{\text{rad}} \sim 3000$ km s $^{-1}$ (Richard et al. 2010). However, the redshifts of the northern and southern BCGs were found to be $z_{\text{N}} = 0.3780$ and $z_{\text{S}} = 0.3733$, respectively, which implies a relative velocity of only $V_{\text{rad}} \sim 1024$ km s $^{-1}$ at the redshift of A370 (Lagattuta et al. 2019). It is unlikely that the relative velocity of the BCGs to the dark-matter center of their respective host cluster would be larger than ~ 1000 km s $^{-1}$. In the left panel of Figure 2, we show the redshift distribution of 219 cluster member galaxies based on the latest survey (Lagattuta et al. 2019). We found no significant peaks around the redshifts of the two BCGs (0.3733 and 0.3780; vertical solid lines), regardless of the chosen bin size (see the

solid and dashed histograms in Figure 2). The dashed vertical line marks the redshift of the cluster (0.3750). In the right panel of Figure 2, we display the distribution of relative radial velocities of the cluster members (solid histogram) and that from our best model (dashed histogram; see Section 4). The corresponding Gaussian fit to the observed velocity distribution is shown with the solid curve. The dispersion of the observed radial velocity distribution from a Gaussian fit is $\sigma_{\text{obs}} \approx 1795$ km s $^{-1}$. Since we do not find any peaks around the redshifts of the BCGs, we adopt $V_{\text{rad}} = 1024$ km s $^{-1}$, the relative radial velocity of the two BCGs, and assume a large uncertainty of $\pm 30\%$ in the relative velocity of the two cluster components.

3. MODELING A370 USING FLASH

3.1. Simulation Set Up

We model A370 in 3D using an Eulerian N -body/hydrodynamical code FLASH developed at the Center for Astrophysical Thermonuclear Flashes at the University of Chicago (Fryxell et al. 2000; Ricker 2008). FLASH is a publicly available Adaptive Mesh Refinement (AMR) code, which can be run in parallel computer architectures based on CPUs. We include dark matter and gas self-consistently taking the gravity of both components into account.

We modeled A370 as a binary merger assuming spherical symmetry for the initial components. Since the initial memory of the halo asphericity will be completely lost after two core passages, we do not expect to be able to recover the initial asphericity of dark matter halos. We adopted a box size of 19.4 Mpc on a side. The highest resolution, 19 kpc, was reached at high density regions (cluster centers), contact discontinuities, merger shocks, and in turbulent regions (turbulence usually sets the refinement to its maximum in hydrodynamical simulations). We chose a 3D Cartesian coordinate system, x, y, z , with the main plane of the collision (containing the centers of the clusters and the initial velocity vectors of the infalling cluster) placed in the $z = 0$ plane. For any given relative velocity vector, we assign velocities of the two components to set the total momentum of the system to zero to keep the clusters in the simulation box. This was important because we ran our simulations past the third core passage, which typically takes several giga years. The initial velocities of the main (more massive) and the infalling (less massive) cluster were parallel to the z -axis, pointing to the $-z$ and $+z$ directions, respectively. Our simulations were semi-

adiabatic; only the most important non-adiabatic process in merging clusters, shock heating, was included using a shock capturing scheme (included in FLASH). Other non-adiabatic effects, such as radiative cooling and heating (e.g., supernova and AGN feedback), may be safely ignored because the cooling time is very long in the intracluster gas in our simulated clusters and the energy input from heating is insignificant relative to the energetics of the collision.

The initial models of the colliding clusters were assumed to have spherical geometry with cut offs of the dark-matter and gas density at the virial radius, R_{vir} . We assumed an NFW profile for the radial dark-matter distribution,

$$\rho_{\text{DM}}(r) = \frac{\rho_s}{(r/r_s)(1+r/r_s)^2}, \quad (1)$$

where ρ_s is the characteristic density parameter, $r_s = R_{\text{vir}}/c_{\text{vir}}$ is the characteristic radius at which $d \ln \rho_{\text{DM}}(r)/d \ln r = -2$, with c_{vir} the concentration parameter. The gas density was assumed to have a β -model profile,

$$\rho_{\text{gas}}(r) = \frac{\rho_0}{[1 + (r/r_{\text{core}})^2]^{3\beta/2}} \quad (2)$$

where r_{core} is the core radius, ρ_0 is the central density parameter, and β determines the fall off of the gas density at large radii. We assumed $\beta = 1$, as suggested by cosmological simulations for the large scale distribution of the intracluster gas in relaxed clusters (derived excluding filaments; for details see Molnar et al. 2010). We used a gas mass fraction of $f_{\text{gas}} = 0.12$ (e.g., Vikhlinin et al. 2006; Umetsu et al. 2009; Tian et al. 2020), and assumed, as an approximation, that the galaxies are collisionless and follow the dark-matter distribution.

We determined the initial gas temperature distribution as a function of the cluster-centric radius, $T(r)$, assuming hydrostatic equilibrium and $\gamma = 5/3$ for the ideal gas equation of state. It is more difficult to model a stable dark-matter density distribution. The velocity field has to be set up initially to provide the required stable density distribution dynamically as the dark-matter particles move around on their orbits. With the assumptions of spherical density distribution and isotropic velocity dispersion, the Jeans equation can be solved for the amplitude of the velocity dispersion, $\sigma_v(r)$, as a function of r (Łokas & Mamon 2001). We obtain the amplitudes of the velocities for dark-matter points at radius r by sampling the $\sigma_v(r)$ distribution derived from the Jeans equation and choose an angle from an isotropic distribution, which is referred to as the local Maxwellian approximation. For further details of the set up of our simulations, see Molnar et al. (2012).

3.2. FLASH Simulations

The large masses of the two cluster components and the long time to reach the third core passage make a systematic search in the full parameter space (i.e., the initial masses, concentration parameters, infall velocity, and impact parameter) unfeasible using currently available conventional high-speed computing nodes based on CPUs. Therefore, to reduce the computer demand, we inspected simulations from our extensive runs of existing simulations and performed new simulations by reducing the parameter space to find a reasonable model for A370.

Taking advantage of the north-south symmetry of the mass distribution based on gravitational lensing, which suggests that the mass ratio M_1/M_2 is close unity (Section 2.3), we

Table 1
Input parameters used in our FLASH simulations.

ID ^a	M_1^b $10^{15} M_\odot$	c_1^c $10^{15} M_\odot$	M_2^b	c_2^c	P^d kpc	V_{in}^e km s^{-1}
RP100V3.0	1.7	7.0	1.6	7.0	100	3000
RP100V3.5	1.7	7.0	1.6	7.0	100	3500
RP100V3.7	1.7	7.0	1.6	7.0	100	3700
RP100V4.0	1.7	7.0	1.6	7.0	100	4000
RP200V3.5	1.7	7.0	1.6	7.0	200	3500
RP200V3.0	1.7	7.0	1.6	7.0	200	3000
RP300V3.0	1.7	5.0	1.6	5.0	300	3000
RP400V2.0	1.7	5.0	1.6	5.0	400	2000
RP400V3.0	1.7	6.0	1.6	7.0	400	3000
RP100V3.5a	1.7	5.0	1.6	5.0	100	3500
RP100V3.5b	1.7	6.0	1.6	6.0	100	3500
RP100V3.5c	1.7	8.0	1.6	8.0	100	3500

^a IDs of the runs

^b Virial masses M_{vir} of the main and the infalling cluster (M_1 and M_2)

^c Concentration parameter c_{vir} for each component (c_1 and c_2).

^d Impact parameter.

^e Infall (relative 3D) velocity.

fixed the virial masses at $M_1 = 1.7 \times 10^{15} M_\odot$ and $M_2 = 1.6 \times 10^{15} M_\odot$. Here we break the unphysical perfect symmetry by choosing $M_1/M_2 \neq 1$. A slight change of the total mass, or mass ratio, would not cause significant change in the projected X-ray morphology and other parameters, while the best epochs and view angles would be somewhat different. By inspecting the merging cluster simulations in our extensive data base and performing additional simulations, we find that significantly different initial masses do not provide a good match with the observations. Fixing the initial masses allows us to reduce the parameter space to a manageable level. We carried out a series of FLASH simulations varying the impact parameter, the infall velocity, and the concentration parameters of our model. Our aim was to find a physical model for A370 with a reasonable agreement with the multi-wavelength observations.

We used the following constraints to find the best model for A370: (i) Peak offset in the projected dark matter distribution $D_{\text{proj}} = 206$ kpc (Straight et al. 2018): since the uncertainty in D_{proj} , ~ 30 kpc, results only in a small change in the rotation angles and the noise fluctuations in the mock *Chandra* images are larger than the change in the X-ray surface brightness, we kept D_{proj} fixed at this value; (ii) Relative radial velocity $V_{\text{rad}} = 1024 \text{ km s}^{-1}$: we allowed a $\pm 30\%$ variation in V_{rad} (Section 2.3); (iii) SZ amplitude $Y_{2500} = 0.91 \times 10^{-10}$ ster based on our Bolocam measurements (Czakon et al. 2015), allowing a 2σ offset (Section 2.2); (iv) X-ray morphology: we focused on the positions of the X-ray peaks and their offsets from the mass peaks because of the low counts in the outer regions. The location of the main X-ray peak was required to lie between the two mass centers, about half way with a small offset to the west, with an extension toward the southern mass peak, and the secondary peak to lie close to the northern mass center with a small offset toward south-west. Our model constraints were based on quantitative criteria, except for those based on the X-ray morphology.

From our simulations we choose those epochs for which a viewing angle that satisfies all the three quantitative criteria ((i), (ii), and (iii)) can be found. Then, the best match with observations was found by inspecting visually the simulated *Chandra* images based on our criteria for the X-ray morphol-

ogy (see the next section for a description of our method to generate mock *Chandra* observations). Since our FLASH simulations have no feedback, heating, and cooling processes, we use the integrated SZ amplitude, Y_{2500} , to constrain the physical state of the gas, which is proportional to the dynamically important quantity, the thermal pressure. The pressure distribution in our simulations is more realistic than other gas quantities because the history of merging clusters is determined mostly by hydrodynamics and the balance between pressure and gravitational forces.

Our procedure of using simulations was as follows: We used a trial-and-error approach to run simulations and find a set of initial conditions that satisfy our four criteria. A systematic parameter search was not possible because of large parameter space demanding too much computer time. After finding the best match, we ran additional simulations with a range of different initial conditions to constrain the parameter space.

In Table 1, we summarize the initial parameters of our FLASH simulations that are relevant to this paper. This represents a small subset of parameter space that contains our best solution and a few simulations to illustrate the effects of varying the parameters around the values of our best model. Here we did not include the parameters of all merging cluster simulations because it is not informative. The first column contains the IDs of our runs indicated as $RP_{ijk}V_{nm}$, with P_{ijk} the impact parameter in units of kpc and V_{nm} the infall velocity in units of 1000 km s^{-1} . Table 1 also lists the impact parameter P in kpc and the 3D infall velocity V_{in} in km s^{-1} . The infall velocity we adopt is the relative velocity of the two clusters at the time when the two intracluster gas touch as they collide, i.e., when the distance between them is the sum of their virial radii.

3.3. Monte Carlo Simulations of X-ray Images

We have used Monte Carlo simulations to generate mock *Chandra* X-ray surface brightness images. We defined our Cartesian coordinate system as the $z-x$ plane being in the plane of the sky and the z axis connecting the two dark-matter mass centers pointing to the direction of motion of the infalling cluster. We chose the y axis so that x , y , and z form a right handed coordinate system. At each epoch we considered for output, we rotated the simulated cluster around the z axis by different roll angles φ . We then rotated the cluster out of the plane of the sky around the y axis by a polar angle θ to obtain $D_{\text{proj}} = 206 \text{ kpc}$ between the two dark-matter centers, matching the projected distance derived from gravitational lensing (Strait et al. 2018). All 3D rotations were carried out using the IDL function ROT, which relies on an interpolation scheme to find values at the rotated pixel centers. We derived the 3D distances between the mass peaks based on the particle output from FLASH and calculated the the polar angles θ by requiring the projected distance to be $D_{\text{proj}} = 206 \text{ kpc}$.

We generated mock images of the cluster using the same pixel size, $0.492''$, as the ACIS detectors of *Chandra* (Garmire et al. 2003) by integrating the X-ray emissivity along the line-of-sight (LOS) projected to the same sky coordinates as the observations (the sky coordinates of the observations can be obtained from the corresponding FITS files). We used the X-ray surface brightness image based on our analysis of *Chandra* data to read off the number of background photons per pixel. We generated mock *Chandra* images using Monte Carlo simulations based on adding the number of photons ex-

pected from the cluster and the background. A more detailed description of our methods to generate simulated X-ray surface brightness and mass surface density images can be found in Molnar & Broadhurst (2015). When comparing our mock X-ray surface brightness images to the observed ones, we exclude ACIS chip gaps and keep only the image of the chip that contains the center of A370. We also excise an area around the foreground bright elliptical galaxy for clarity.

4. RESULTS AND DISCUSSION

We show in Figures 3 and 4 the X-ray surface brightness image of A370 derived from *Chandra* data and the images of mock *Chandra* observations based on our FLASH simulations. Here we applied the same smoothing ($5''$) on the observed and simulated images for comparison. The images are $1.14 \text{ Mpc} \times 1.56 \text{ Mpc}$. We used the same color code for all panels and excluded the area containing the foreground elliptical galaxy in the north for clarity. For each mock observation, the epoch and the viewing angle were chosen such that the relative LOS velocity matches $V_{\text{rad}} \sim 750 \text{ km s}^{-1}$ and the locations of the two peaks of the mass surface density are aligned with those observed.³

In general, a viewing angle that produces a projected mass peak separation of $D_{\text{proj}} \sim 206 \text{ kpc}$ and a relative LOS velocity of $V_{\text{rad}} \sim 750 \text{ km s}^{-1}$ may be chosen at a few epochs before and after the core passages, as long as the 3D velocity due to the accelerating or decelerating infalling cluster is greater than $\sim 750 \text{ km s}^{-1}$. We found that projections with a LOS relative velocity of $V_{\text{rad}} \sim 750 \text{ km s}^{-1}$ before/after the first core passage and before the second core passage appear to result in a single bright peak in the X-ray surface brightness, independently of the infall velocity and impact parameter of the collision and the viewing angle. This is illustrated in Figure 4 (see the first panels in the first and second rows). The relative velocities in the simulations at epochs after the third core passage are usually too low to produce the required relative radial velocity. Therefore, we shall focus on simulations at epochs between the second and third core passages.

The first panel of Figure 3 shows the smoothed *Chandra* X-ray image based on our analysis (see Section 2.1). Images shown in the other panels are based on our best simulation run (RP300V3.5) at the best epoch, 0.57 Gyr (6.8 Gyr) after the second (first) core passage with a polar angle of $\theta = 72.4^\circ$ and three different roll angles, namely $\varphi = 0^\circ, -120^\circ$, and -158° . The X-ray morphology with a roll angle of $\varphi = -158^\circ$ provides the best match with the observations. Contrary to the observations, views with roll angles of $\varphi = 0^\circ$ and -120° exhibit two X-ray peaks near their associated mass peaks, but no X-ray peak around half way between them.

The best model is provided by our RP100V3.5 run at an epoch of 0.57 Gyr after the second core passage and just before the third core passage, with a polar angle of $\theta = 72.4^\circ$ and a roll angle of $\varphi = -158^\circ$ (see the third panel in Figure 3). The main X-ray peak is located between the two mass centers, about half way with a small offset to the west. It shows an extension toward the southern mass peak and the secondary peak is close to the northern mass center, with a small offset toward south-west. With this viewing angle, the two cluster components of RP100V3.5 has a relative radial velocity of $V_{\text{rad}} = 960 \text{ km s}^{-1}$ and an integrated SZ amplitude of $Y_{2500} = 1.2 \times 10^{-10} \text{ ster}$.

³ This can be achieved with a proper choice of the polar angle, θ , if the 3D separation is $\geq 206 \text{ kpc}$ at a given epoch.

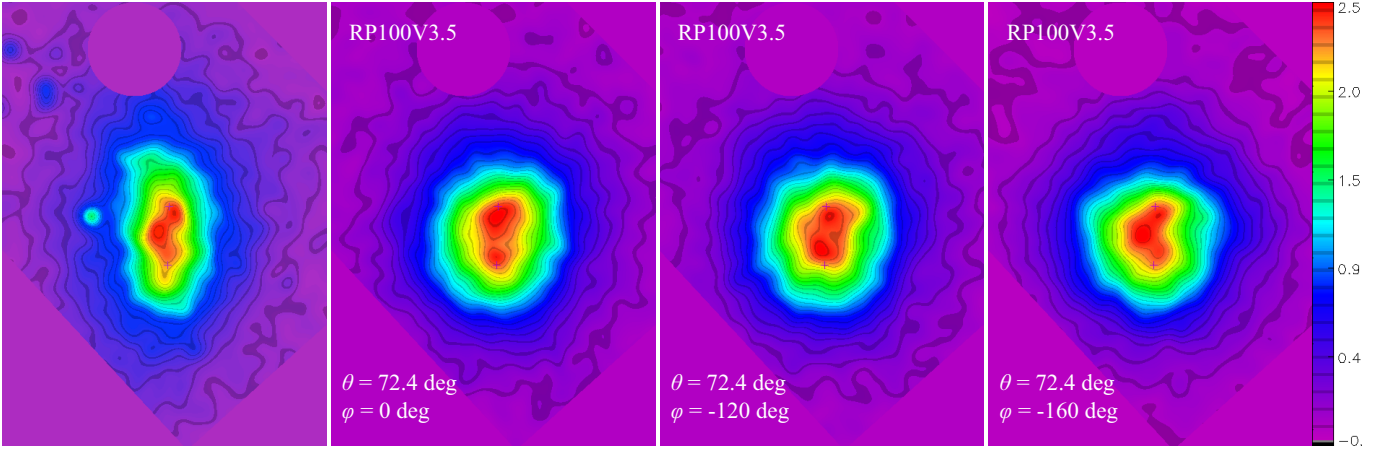


Figure 3. X-ray surface brightness images of A370 based on *Chandra* observations and our simulations at the best epoch and with different viewing angles. The images are $1.14 \text{ Mpc} \times 1.56 \text{ Mpc}$. The two black crosses in each panel mark the peaks of the mass surface density distribution. Left to right: first panel: *Chandra* X-ray image. The area around the bright X-ray source in the north, a foreground elliptical galaxy, was masked in the observed image and also in the simulated images for easier comparison. Second, third, and fourth panels: X-ray images based on our best simulation run (RP100V3.5) at the best epoch after the second core passage, with different roll angles ($\varphi = 0^\circ, -120^\circ, -158^\circ$). The epochs and the viewing angles were chosen to match the positions of the dark-matter centers, the relative radial velocities of the two merging clusters with the observations, and, if possible, to resemble the observed X-ray morphology.

We show in the right panel of Figure 2 (dashed histogram) the distribution of relative radial velocities constructed from our best model. The corresponding Gaussian fit to our simulated histogram is shown with the dashed curve. We obtain a velocity dispersion of $\sigma_{\text{sim}} \approx 1654 \text{ km s}^{-1}$ based on our best model, which agrees well within 10% with the observed value ($\sigma_{\text{obs}} \approx 1795 \text{ km s}^{-1}$; see Section 2.3).

We thus conclude that, our simulation (RP100V3.5) with total virial masses of $M_1 = 1.7 \times 10^{15} M_\odot$ and $M_2 = 1.6 \times 10^{15} M_\odot$, an initial impact parameter of $P \sim 100 \text{ kpc}$, a 3D infall velocity of $V_{\text{in}} \sim 3500 \text{ km s}^{-1}$, and concentration parameters of $c_1 = 6$ and $c_2 = 6$ is the best dynamical model for A370. Our best model is in agreement with an earlier interpretation of multiwavelength observations of A370, that is, it is a massive post major merger with $M_1/M_2 \sim 1$. Moreover, the distribution of radial velocities derived from our best model is very similar to that observed in A370 (compare the dashed and solid histograms in the left panel of Figure 2). This agreement provides an independent confirmation of the large mass derived from weak lensing by Umetsu et al. (2011a,b).

We note that the shape of the outer X-ray brightness distribution from our best model is rounder than the observed one, which is a consequence of a shallower fall off of the gas density distribution than that of A370. Here we did not aim to improve the fit of the outer regions, because it would require an even more extensive search in an extended parameter space including the outer density slope of the initial clusters, which would increase the computer time significantly. However, on the basis of our extensive simulations, we do not expect a significant difference in the cluster core regions from changing the slope in the outer regions with much lower gas densities.

We have also performed a few simulations using different values of P , V_{in} , and c_{vir} to derive crude constraints on our best initial parameters (see Table 1 for the list of parameters of simulations discussed in our paper). Specifically, we ran simulations with the infall velocity V_{in} in the range of 2000 to 4000 km s^{-1} , the impact parameter P from 100 to 400 kpc, and the concentration parameter c_{vir} from 5 to 8 to cover a representative range of parameter space. We did not perform simulations with zero impact parameter because that would result in an X-ray morphology with axial symmetry contrary

to the observations. We chose $V_{\text{in}} = 2000 \text{ km s}^{-1}$ for the lower limit of the infall velocity because mergers with smaller infall velocities result in an integrated SZ effect (Y_{2500}) that is too large to match the Bolocam measurements. An infall velocity of $V_{\text{in}} = 4000 \text{ km s}^{-1}$ already results in an unacceptably long time interval between the first and second core passages (longer than the age of the universe) for highly massive clusters. Since such massive clusters have lower concentration parameters on average, we chose the lower limit of 5 and ran simulations within the range $c_{\text{vir}} \in [5, 8]$. A full parameter search is not feasible with CPU clusters due to the large demand on computer resources.

In Figure 4, we show mock *Chandra* images based on our simulations between the second and third core passages that do not provide the best match with the observations. Most of the initial parameters were the same as in our best model (RP100V3.5), but we changed one or two parameters for each run to show how the changes impact the X-ray morphology (for the initial parameters, see Table 1). The first panel in the first row shows our simulation with an impact parameter changed to $P = 200 \text{ kpc}$ (RP200V3.5) at an epoch 1.1 Gyr (8.7 Gyr) after the second (first) core passage. The X-ray morphology shows only one bright peak. Thus, it does not match the observations although it has an integrated SZ amplitude of $Y_{2500} = 1.1 \times 10^{-10}$ ster, which agrees with the Bolocam constraint.

The second panel displays our simulation with the infall velocity changed to $V_{\text{in}} = 3000 \text{ km s}^{-1}$ (RP100V3.0) at an epoch 0.68 Gyr (3.4 Gyr) after the second (first) core passage. The X-ray surface brightness has two peaks with similar amplitudes (but no dominant peak) and no extension to the southern mass center. Moreover, it also has a somewhat large integrated SZ amplitude, $Y_{2500} = 1.4 \times 10^{-10}$ ster.

In the third and fourth panels, we show X-ray images based on our simulation with an infall velocity of $V_{\text{in}} = 3700 \text{ km s}^{-1}$ (RP100V3.7) at two different epochs, 0.32 Gyr (11 Gyr) and 1.4 Gyr (12 Gyr) after the second (first) core passage. Again, the X-ray morphologies do not match with the observations: the image in the third panel shows a single peak, while the fourth panel shows two peaks with similar amplitudes and no extension toward the southern mass peak. The integrated SZ amplitudes are $Y_{2500} = 2.6 \times 10^{-10}$ ster and

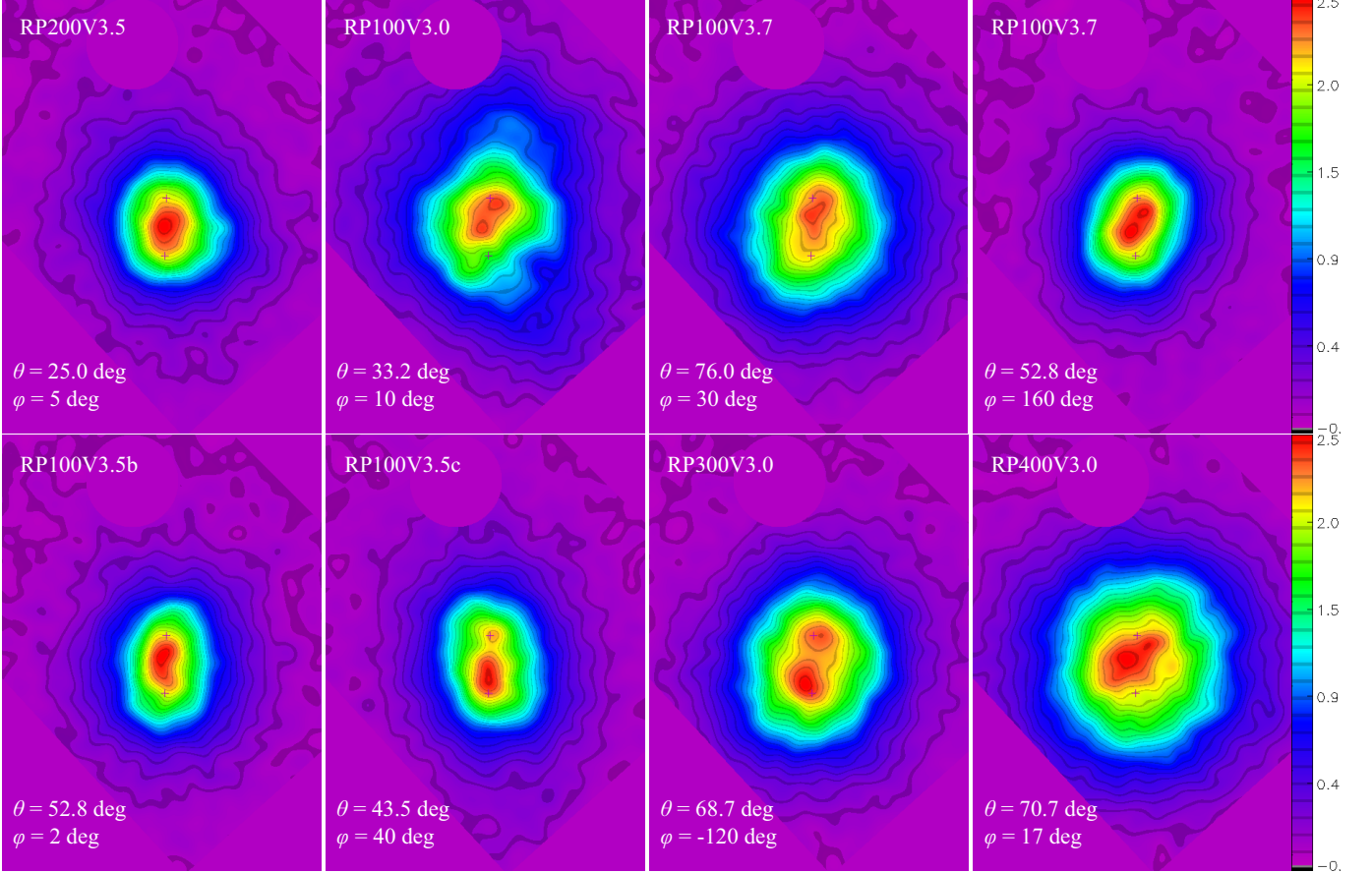


Figure 4. X-ray surface brightness images of A370 based on our simulations. Most of the initial parameters were the same as in our best model, but we changed one or two parameters for each run (see Table 1) to show how the changes impact the X-ray morphology. The epochs and the viewing angles were chosen to match the observations and, if possible, to resemble the observed X-ray morphology. From left to right: First row: first panel: our simulation with an impact parameter of $P = 200$ kpc (RP200V3.5); second panel: our simulation with an infall velocity of $V_{\text{in}} = 3000 \text{ km s}^{-1}$ (RP100V3.0); third and fourth panels: our simulation with an infall velocity of $V_{\text{in}} = 3700 \text{ km s}^{-1}$ (RP100V3.7) at two different epochs after the second core passage. Second row: first panel: the concentration parameters are changed to $c_1 = c_2 = 6$ (RP100V3.5b); second panel: the concentration parameters are changed to $c_1 = c_2 = 8$ (RP100V3.5c); third panel: the impact parameter is changed to $P = 300$ kpc and the infall velocity to $V_{\text{in}} = 3000 \text{ km s}^{-1}$ (RP300V3.0); fourth panel: the impact parameter is changed to $P = 400$ kpc, the infall velocity to $V_{\text{in}} = 3000 \text{ km s}^{-1}$, and the concentration parameters to $c_1 = 6$ and $c_2 = 7$ (RP400V3.0).

9.4×10^{-11} ster at these epochs, and thus the first epoch can be excluded based on its large integrated SZ amplitude as well.

The first and second panels in the second row of Figure 4 display our simulations with concentration parameters $c_1 = c_2 = 6$ (RP100V3.5b) and $c_1 = c_2 = 8$ (RP100V3.5c), while the other initial parameters are the same as those of our best simulation. These images are shown at epochs of 0.16 Gyr (7.8 Gyr) and 0.92 Gyr (6.4 Gyr) after the second (first) core passage. The X-ray morphologies of these images do not provide a good match with the observations, even though they satisfy all other requirements including their integrated SZ amplitude, $Y_{2500} = 1.0$ and 1.1×10^{-10} ster, which agree with the Bolocam constraint.

The third panel in the second row shows our simulations with an impact parameter of $P = 300$ kpc and an infall velocity of $V_{\text{in}} = 3000 \text{ km s}^{-1}$ (RP300V3.0), at an epoch 0.20 Gyr (4.3 Gyr) after the second (first) core passage. The X-ray morphology of this run shows two X-ray peaks, whereas the morphology does not provide a good match with the observations. The fourth panel displays our simulations with an impact parameter of $P = 400$ kpc, an infall velocity of $V_{\text{in}} = 3000 \text{ km s}^{-1}$, and concentration parameters of $c_1 = 6$ and $c_2 = 7$ (RP400V3.0) at an epoch 0.32 Gyr (4.2 Gyr) after the second (first) core passage. Again, we find two X-

ray peaks, but the morphology does not match the observations. These two runs can be excluded based on their large integrated SZ amplitudes, $Y_{2500} = 2.1$ and 2.4×10^{-10} ster, which are more than twice as large as the Bolocam constraint, $Y_{2500} = 0.9 \times 10^{-10}$ ster.

On the basis of our simulations with fixed initial masses ($M_1 = 1.7 \times 10^{15} M_{\odot}$ and $M_2 = 1.6 \times 10^{15} M_{\odot}$) and different impact parameters, infall velocities, and concentration parameters, we can provide a crude estimate on the uncertainties of our best model parameters as $P = 100_{-100}^{+100}$ kpc, $V_{\text{in}} = 3500_{-500}^{+200} \text{ km s}^{-1}$, and $c_1 = 6 \pm 1$ and $c_2 = 6 \pm 1$. However, we should consider these initial conditions only as a guide to set up the conditions for the second core passage, since our simulations have high fidelity only from around the second core passage until the best epoch. That is why we displayed the time elapsed from the first core passage for our simulations only in parentheses. The reason for this is that, as usually done in controlled binary merger simulations, the expansion of the universe and mass accretion from the surrounding large-scale structure are ignored (e.g., Ricker & Sarazin 2001; Ritchie & Thomas 2002; Poole et al. 2007; McCarthy et al. 2007; ZuHone et al. 2011; for a discussion, see Molnar 2016). This is a good approximation for a few Gyrs, but not for a significant fraction of the age of the universe, such as 5–

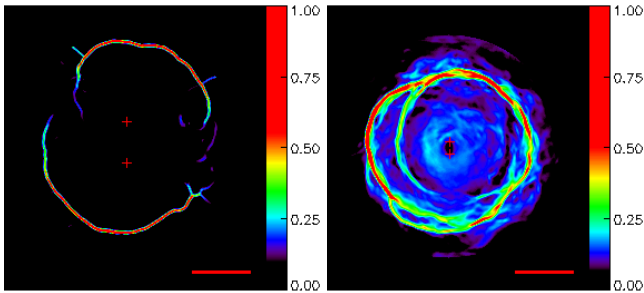


Figure 5. Images of shock positions (red curves) based on our best simulation run (RP100V3.5) at the best epoch. The two red crosses mark the peak locations of the mass surface density distribution. The length of the horizontal red line is 1 Mpc. Left panel: magnitude of the pressure gradient in a 2D cut through a plane containing the two cluster centers before rotation out of the plane of the sky. Right panel: the magnitude of the pressure gradient of the projected pressure based on our best simulation with the best viewing angle (Section 4).

10 Gyrs, which is the time scale of our simulations from the first to the second core passage, due to the large masses and infall velocities we had to assume. On a time scale of a significant fraction of the age of the universe, the expansion of the background and the mass accretion of clusters cannot be ignored. A study of the dynamics of A370 through its evolution would need a cosmological N -body/hydrodynamical simulation, which would incorporate these effects naturally. This could be done, for example, using constrained realizations of Gaussian random fields (Hoffman & Ribak 1991), or one of its variants (e.g., Roth et al. 2016; Rey & Pontzen 2018; Sawala et al. 2020). However, this is out of the scope of our paper.

In general, during each core passage, outgoing shockwaves are generated in the central region of merging galaxy clusters. We show in Figure 5 the outgoing shocks generated after the second core passage based on our best simulation (RP100V3.5) at the best epoch. We identified the shocks using the magnitude of the pressure gradient. The locations of large gradients in the pressure delineate the shock surfaces. In these images, the red curves show the location of the shocks. The red crosses mark the dark-matter centers and the horizontal red bars indicate the physical scale of 1 Mpc.

In the left panel of Figure 5, we show the magnitude of the pressure gradient in a two-dimensional (2D) cut through the centers of the two components, before the rotation of the system out of the plane of the sky. This image shows the physical (not projected) locations of the shocks. The two shocks generated after the second core passage can be clearly seen. The shocks are moving outward from the center. Using this 2D pressure cut, we can derive the Mach numbers of these shocks to obtain $\mathcal{M} \sim 3.2$. At this epoch, the merging cluster is in an infalling phase, where the two dark-matter components already turned over and are moving toward each other, approaching the third core passage.

In the right panel of Figure 5, we display the magnitude of the projected pressure gradient using our best model, which is rotated out of the plane of the sky with a polar angle of 72.4° . This panel shows where the shocks could be observed. The two well-separated shock waves form entangled circles to the cluster center is on the east side, about 890 kpc away from the center. We note that, owing to projection effects, the change in the projected pressure is not equal to the physical pressure change due to the shock. The Mach number derived from the pressure drop in this projection is $\mathcal{M} \sim 1.2$, much less than the physical Mach number. We expect that observations of

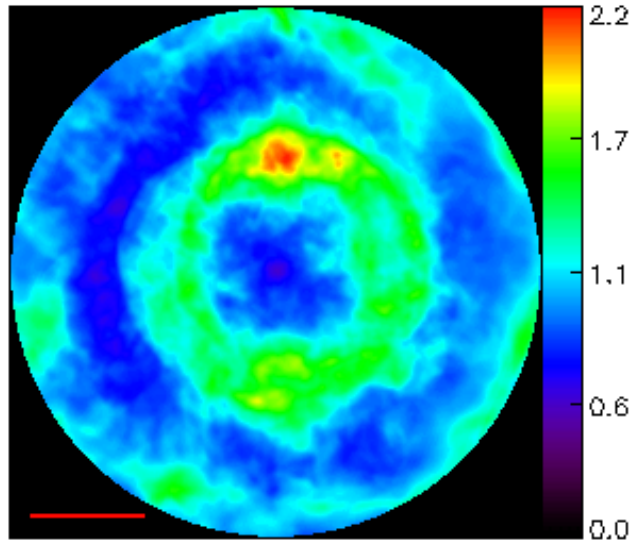


Figure 6. The gas mass surface density ratio, $\Sigma_{\text{best}}/\Sigma_{2\text{CP}}$ (best epoch over second core passage), based on our best model (RP100V3.5) at the best viewing angle within 2.5 Mpc from the cluster center. The red horizontal bar marks 1 Mpc.

this outgoing shock would measure a Mach number close to this value (for a discussion on how much bias is caused by projection effects in the Mach numbers derived from X-ray observations, see, e.g., Molnar & Broadhurst 2017). The position of the closest shock in the east is in rough agreement with the position of the X-ray surface brightness edge we found by reanalyzing the *Chandra* observations of A370 (at ~ 690 kpc; Section 2.1; see Figure 5b). Our simulations suggest that the X-ray surface brightness edge found in A370 on the east from the cluster center is an outgoing shock generated after the second core passage. According to our best model, the outgoing shock on the west of the cluster center is located much farther out than the X-ray surface brightness edge found by Botteon et al. (2018). Reanalyzing the *Chandra* data, we found no significant X-ray edge on the east from the cluster center, which is in agreement with our best model.

As a result of the outgoing shocks generated after the second core passage, the gas density decreases in the central region. In a later phase, the gas falls back toward the center. We display in Figure 6 the ratio $\Sigma_{\text{best}}/\Sigma_{2\text{CP}}$ between the gas mass surface density Σ_{best} at the best epoch (i.e., our best model) and that $\Sigma_{2\text{CP}}$ at the epoch of the second core passage based on our best run (RP100V3.5). These projected maps are obtained using the viewing angle of our best model within 2.5 Mpc from the cluster center. The red horizontal bar in the lower-left corner marks a scale of 1 Mpc, which is about the size of the BOLOCAM extraction region around the cluster center ($R \lesssim R_{2500}$; central blue region). At the best epoch after the second core passage, the cluster passed the second turnover, while the gas is still moving outward as a result of the shock, which is located about 1–2 Mpc from the cluster center (see Figure 5). Accordingly, the gas is depleted in the central area where $\Sigma_{\text{best}}/\Sigma_{2\text{CP}} \sim 0.7$ (dark blue region). This depletion of the gas from the central part of the system explains why the X-ray emission and SZ amplitude of this cluster is well below those suggested by cluster mass scaling relations (Section 1).

We have used our existing library of binary merging cluster simulations performed in our previous work and carried out self-consistent N -body/hydrodynamical simulations with FLASH to study the dynamical state of the massive merging cluster A370. The cluster is a superlens system characterized by its large Einstein radius. Our simulations were constrained by X-ray, SZ-effect, gravitational lensing, and optical spectroscopic observations. Specifically, we utilized the locations of the two mass peaks derived from strong gravitational lensing (Strait et al. 2018), the X-ray morphology (Section 2.1), the relative LOS velocity (Section 2.3), and the amplitude of the integrated SZ effect (Section 2.2; Czakon et al. 2015).

We performed FLASH simulations by fixing the masses of the two cluster components based on weak- and strong-lensing measurements (Umetsu et al. 2011a). We used different impact parameters, infall velocities, and concentration parameters to find the best match with the multi-wavelength observations. We found that our best model with masses of $M_1 = 1.7 \times 10^{15} M_\odot$ and $M_2 = 1.6 \times 10^{15} M_\odot$, an impact parameter of $P = 100$ kpc, an infall velocity of $V_{\text{in}} = 3500 \text{ km s}^{-1}$, and concentration parameters of $c_1 = 6$ and $c_2 = 6$ can explain the main features of the X-ray morphology and the mass surface density and simultaneously satisfy the constraints from the observed relative LOS velocity and the integrated SZ amplitude. Moreover, our best model reproduces the observed velocity dispersion of cluster member galaxies, which supports the large total mass of A370 derived from weak lensing. Our results strongly suggest that A370 is a post major merger observed 0.57 Gyr after the second core passage, just before the third core passage.

It is intriguing to note that, similar to the case of A370, Cl0024+1654 is another superlens cluster at $z = 0.395$ that is very faint in X-ray and SZ signals (Umetsu et al. 2011a,b). A careful interpretation of X-ray, lensing, and dynamical data based on FLASH simulations suggests that Cl0024+1654 is also a post major merger occurring along the line of sight, viewed approximately 2–3 Gyr after impact before the gas has recovered (Umetsu et al. 2010).

Our simulations represent the first attempt to model one of the most massive dynamically active merging galaxy clusters, A370, using dedicated self-consistent N -body/hydrodynamical simulations. In order to improve our dynamical model for A370, deeper X-ray observations would be necessary to verify the positions of the main and secondary peaks, obtain a spatially resolved temperature distribution of the intracluster gas, and verify the shock feature in the east from the cluster center. Moreover, a detailed optical spectroscopic study would be needed to precisely determine the relative LOS velocity of the two main merging components. With these proposed new observations a more extensive parameter search would be worth while to pursue, which is more likely feasible using GPU clusters.

We thank the referee for a thorough reading of our manuscript, and for comments and suggestions, which made the presentation of our results clearer. We are grateful to J. Richard and D. J., Lagattuta for providing us with the electronic table of the cluster redshifts from their latest survey of A370 and helping with analyzing the data. The code FLASH used in this work was in part developed by the DOE-supported ASC/Alliance Center for Astrophysical Thermonuclear Flashes at the University of Chicago. We carried out our simulations using the high performance computer facility at the Academia Sinica Institute of Astronomy and As-

trophysics. This work was supported in part by the Ministry of Science and Technology of Taiwan (grant MOST 106-2628-M-001-003-MY3) and by Academia Sinica (grant AS-IA-107-M01).

REFERENCES

- Arnaud, K. A. 1996, *Astronomical Data Analysis Software and Systems V*, 101, 17
- Botteon, A., Gastaldello, F., & Brunetti, G. 2018, *MNRAS*, 476, 5591
- Broadhurst, T., Umetsu, K., Medezinski, E., Oguri, M., & Rephaeli, Y. 2008, *ApJL*, 685, L9
- Coe, D., Salmon, B., Bradač, M., et al. 2019, *ApJ*, 884, 85
- Czakon, N. G., Sayers, J., Mantz, A., et al. 2015, *ApJ*, 806, 18
- Diego, J. M., Schmidt, K. B., Broadhurst, T., et al. 2018, *MNRAS*, 473, 4279
- Fruscione, A., McDowell, J. C., Allen, G. E., et al. 2006, *Proc. SPIE*, 62701V
- Fryxell, B., et al. 2000, *ApJS*, 131, 273
- Garmire, G. P., Bautz, M. W., Ford, P. G., Nousek, J. A., & Ricker, G. R., Jr. 2003, *Proc. SPIE*, 4851, 28
- Hoffman, Y., & Ribak, E. 1991, *ApJL*, 380, L5
- Kalberla, P. M. W., Burton, W. B., Hartmann, D., et al. 2005, *A&A*, 440, 775
- Kitayama, T., & Suto, Y. 1996, *ApJ*, 469, 480
- Kochanek, C. A. 1990, *MNRAS*, 247, 135
- Lagattuta, D. J., et al. 2017, *MNRAS*, 469, 3946
- Lagattuta, D. J., Richard, J., Bauer, F. E., et al. 2019, *MNRAS*, 485, 3738
- Lokas, E. L., & Mamon, G. A. 2001, *MNRAS*, 321, 155
- Lotz, J. M., et al. 2017, *ApJ*, 837, 97
- McCarthy, I. G., Bower, R. G., Balogh, M. L., et al., 2007, *MNRAS*, 376, 497
- Medezinski, E., Broadhurst, T., Umetsu, K., et al. 2010, *MNRAS*, 405, 257
- Miralda-Escude, J. 1991, *ApJ*, 370, 1
- Molnar, S. 2016, *Front. Astron. Space Sci.*, 2, 7
- Molnar, S. M., & Broadhurst, T. 2015, *ApJ*, 800, 37
- Molnar, S. M., & Broadhurst, T. 2017, *ApJ*, 841, 46
- Molnar, S. M., & Broadhurst, T. 2018, *ApJ*, 862, 112
- Molnar, S. M., Broadhurst, T., Umetsu, K., et al. 2013a, *ApJ*, 774, 70
- Molnar, S. M., Chiu, I.-N. T., Broadhurst, T., & Stadel, J. G. 2013b, *ApJ*, 779, 63
- Molnar, S. M., Hearn, N. C., & Stadel, J. G. 2012, *ApJ*, 748, 45
- Molnar, S. M., et al. 2010, *ApJ*, 723, 1272
- Navarro, J. F., Frenk, C. S., & White, S. D. M. 1997, *ApJ*, 490, 493
- Poole, G. B., Fardal, M. A., Babul, A., et al., 2006, *MNRAS*, 373, 881
- Pratt, G. W., Croston, J. H., Arnaud, M., & Böhringer, H. 2009, *A&A*, 498, 361
- Rey, M. P., & Pontzen, A. 2018, *MNRAS*, 474, 45
- Richard, J., Kneib, J.-P., Limousin, M., Edge, A., & Jullo, E. 2010, *MNRAS*, 402, L44
- Ricker, P. M. 2008, *ApJS*, 176, 293
- Ricker, P. M. & Sarazin, C. L. 2001, *ApJ*, 561, 621
- Ritchie, B. W., & Thomas, P. A. 2002, *MNRAS*, 329, 675
- Roth, N., Pontzen, A., & Peiris, H. V. 2016, *MNRAS*, 455, 974
- Sawala, T., Jenkins, A., McAlpine, S., et al. 2020, *arXiv e-prints*, arXiv:2003.04321
- Schmidt, K. B., et al. 2014, *ApJ*, 786, 57
- Soucail, G. 1987, *The Messenger*, 48, 43
- Soucail, G., Mellier, Y., Fort, B., Mathez, G., & Cailloux, M. 1988, *A&A*, 191, L19
- Steinhardt, C. L. et al. 2020, *ApJS*, 247, 64
- Strait, V., Bradač, M., Hoag, A., et al. 2018, *ApJ*, 868, 129
- Tian, Y., Umetsu, K., Ko, C.-M., Donahue, M., & Chiu, I.-N. 2020, *arXiv:2001.08340*
- Treu, T., et al. 2015, *ApJ*, 812, 114
- Tyson, J., Valdes, F., Wenk, R. A. 1990, *ApJL*, 349, L1.
- Ueda, S., Ichinohe, Y., Kitayama, T., et al. 2019, *ApJ*, 871, 207
- Umetsu, K., Tada, M., & Futamase, T. 1999, *PThPS*, 133, 53
- Umetsu, K., Birkinshaw, M., Liu, G.-C., et al. 2009, *ApJ*, 694, 1643
- Umetsu, K., Medezinski, E., Broadhurst, T. et al. 2010, *ApJ*, 714, 1470
- Umetsu, K., Broadhurst, T., Zitrin, A., Medezinski, E., & Hsu, L.-Y. 2011a, *ApJ*, 729, 127
- Umetsu, K., Broadhurst, T., Zitrin, A., E. Medezinski, D. Coe, & M. Postman 2011b, *ApJ*, 738, 41
- Vikhlinin, A., Kravtsov, A., Forman, W., et al. 2006, *ApJ*, 640, 691
- ZuHone, J. A., 2011, *ApJ*, 728, 54